European Journal of Mechanics / A Solids 101 (2023) 105076

Contents lists available at ScienceDirect

European Journal of Mechanics / A Solids

journal homepage: www.elsevier.com/locate/ejmsol

Numerical estimation via remeshing and analytical modeling of nonlinear elastic composites comprising a large volume fraction of randomly distributed spherical particles or voids

H. Luo, Z. Hooshmand-Ahoor, K. Danas, J. Diani *

LMS, C.N.R.S., École Polytechnique, Institut Polytechnique de Paris, 91128 Palaiseau, France

ARTICLE INFO

Keywords:
Homogenization
Particle composites
Finite strain
Finite element
Remeshing
Porous materials

ABSTRACT

We investigate numerically via finite element (FE) simulations and analytically the nonlinear behavior of a soft matrix comprising a large volume fraction (up to 55%) of monodisperse spherical inclusions, which can be either rigid particles or voids. To address the issue of severe mesh distortion at large strains, we employ a successive remeshing and solution mapping technique that allows us to achieve a large macroscopic deformation, with the maximum attained stretch being at least two to three times when compared to that without remeshing. A general algorithm allowing to read complex arbitrary particle geometries is proposed and implemented allowing to remesh a finitely strained domain with randomly distributed inclusions of arbitrary shape. The present simulation results for a neo-Hookean elastic matrix filled with rigid particles show that the nonlinear stress–stretch uniaxial tension response can be well approximated by a neo-Hookean material with an effective shear modulus that depends on the volume fraction of the inclusions. Additionally, a study of the number of particles demonstrates that sixty four monodisperse spheres is a good compromise to reach accurate results for large deformations and maintain a reasonable CPU-time. The FE data serve as a powerful assessment tool for analytical homogenization models. Newly developed and existing models for small and large strains are proposed and assessed, respectively, for both rigid particles and voids. These results fill the gap for large volume fractions of inclusions and serve as a reference for the homogenization of the microstructures of interest.

1. Introduction

Predicting the nonlinear hyperelastic behavior of a soft matrix comprising uniformly distributed hard particles or voids has drawn significant interest in the recent years. Specifically, the macroscopic nonlinear elastic response of heterogeneous materials has been estimated by use of numerical homogenization calculations (Lopez-Pamies et al., 2013; Leonard et al., 2020; Yang et al., 2022) of representative volume elements containing large numbers of inclusions and periodic boundary conditions (Michel et al., 1999; Segurado and Llorca, 2002; Gusev, 2016). In turn, analytical or semi-analytical expressions of hyperelastic strain energy densities characterizing the nonlinear behavior of the homogeneous equivalent materials have been proposed, in the case of rigid particles (Lopez-Pamies and Ponte Castañeda, 2006; Lopez-Pamies et al., 2013; Lefèvre and Lopez-Pamies, 2022) as well as voids (Lopez-Pamies and Ponte Castañeda, 2007; Shrimali et al., 2019), as functions of the strain energy density of the soft matrix and of the volume fraction of inclusions. While such models exhibit a satisfactory accuracy when compared to corresponding FE numerical estimates, most three-dimensional numerical homogenization results in the literature have been limited to volume fractions below 30vol% for rigid particles (Lopez-Pamies et al., 2013; Guo et al., 2014; Leonard et al., 2020; Mukherjee et al., 2020, 2021) and below 40vol% for voids (Zerhouni et al., 2019, 2021; Yang et al., 2022), especially when monodispersed spheres are considered. By contrast, one may also refer to linear elastic simulations for polydisperse, isotropic, porous materials reaching porosities as high as 82vol% (Tarantino et al., 2019), Voronoi-type geometries for muscles with inclusion volume fraction as high as 99vol% or more special idealized, non-isotropic FCC or BCC particle microstructures (Spyrou et al., 2017; Bele et al., 2017), where simulations have been carried out for volume fractions as large as 65vol%.

While finite element (FE) simulations are simpler in porous materials, the main difficulty of conducting finite strain simulations in rigid particle composites at finite strains is a direct consequence of significant mesh distortion in regions between closely packed particles (Lopez-Pamies et al., 2013; Guo et al., 2014). Moreover, when monodisperse

---

* Corresponding author.
E-mail addresses: konstantinos.danas@polytechnique.edu (K. Danas), julie.diani@gmail.com (J. Diani).

https://doi.org/10.1016/j.euromechsol.2023.105076
Received 24 March 2023; Received in revised form 25 May 2023; Accepted 9 July 2023

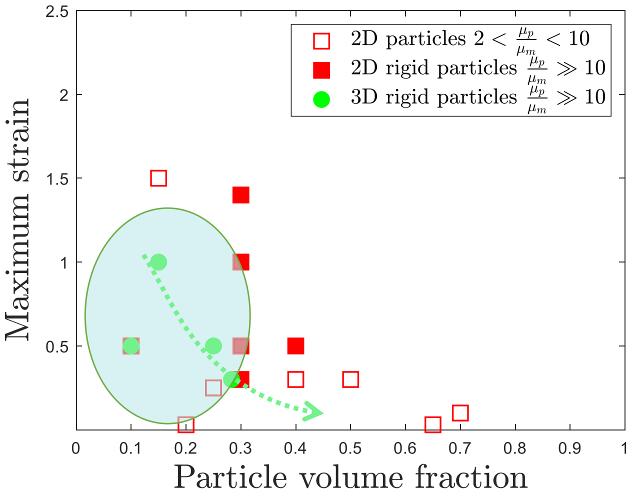

Fig. 1. Maximum effective nominal strain reached in finite element (FE) simulations for uniaxial tensile loading as a function of the particle volume fraction (Brassart et al., 2009; Lopez-Pamies et al., 2013; Jiménez and Pellegrino, 2012; Bouchart et al., 2008; Guo et al., 2007; DeBotton et al., 2006; Yang and Xu, 2009; Khisaeva and Ostoja-Starzewski, 2006; Chi et al., 2015; Meng and Wang, 2015; Leonard et al., 2020; Goudarzi et al., 2015; Guo et al., 2014; Jiménez, 2016; Moraleda et al., 2009).

spherical (or ellipsoidal particles Anoukou et al., 2018) are involved, one is rapidly confronted with the limitation of generating such high volume fraction microstructures (de Francqueville et al., 2019) making even linear elastic simulations highly non-trivial.

As a matter of fact, Fig. 1 illustrates the maximum macroscopic uniaxial tensile strain attained in previous works by numerical FE simulations of composites made of a soft nonlinear elastic matrix filled with either spherical particles in 3D (Guo et al., 2007; de Francqueville et al., 2020; Goudarzi et al., 2015; Lopez-Pamies et al., 2013; Spring and Paulino, 2014) or cylindrical aligned fibers in 2D (Brassart et al., 2009; Jiménez and Pellegrino, 2012; Bouchart et al., 2008; DeBotton et al., 2006; Yang and Xu, 2009; Khisaeva and Ostoja-Starzewski, 2006; Chi et al., 2015; Meng and Wang, 2015; Guo et al., 2014; Jiménez, 2016; Moraleda et al., 2009; Michel et al., 2007). One may observe in this figure the drastic decrease of the maximum effective strain reached as the particle volume fraction increases, rendering difficult, and sometimes impossible, the estimation of the effective nonlinear response of such composites.

The present study aims at extending the current available numerical and analytical homogenization results for particle reinforced and porous nonlinear elastic composites to larger volume fractions (as large as 55vol%). We note that large volume fractions of inclusions have actual material applications such as propellants (de Francqueville et al., 2021), cermets (Bele and Deshpande, 2015; Pickering et al., 2016; Tarantino et al., 2016), muscles (Spyrou et al., 2017, 2019) and closed-cell foams (see for instance Hooshmand-Ahoor et al., 2022). For our numerical simulations, we generate cubic unit cells with randomly distributed monodisperse spheres using the procedure proposed in de Francqueville et al. (2019) that has been proven to work well for monodisperse spheres with volume fractions up to 55vol% (or $c = 0.55$). In turn, the matrix phase is modeled by a soft hyperelastic material and the spheres may be either quasi-rigid or void. While FE simulations are found to be rather straightforward for the porous microstructures in tensile loads, the case of rigid inclusions requires tedious remeshing steps without which the nonlinear response of the heterogeneous material cannot be obtained for the targeted inclusion volume fractions. Remeshing approaches in an updated Lagrangian setting have already been introduced in hyperelasticity (Matsuda et al., 2004; Leger et al., 2014). In this study, we use a similar approach provided by Abaqus standard, which offers an updated Lagrangian mesh-to-mesh solution mapping option such that a solution may be transferred from one mesh to another one. This allows to map the stresses from a severely deformed mesh to a newly generated mesh with improved mesh quality. Such a technique has been already applied successfully to fiber-reinforced elastomers in 2D (Moraleda et al., 2009) and bulk materials in 3D (Rudland et al., 2004; Wang et al., 2011; Yuan et al., 2021).

The case of 3D heterogeneous materials has not been considered yet, perhaps due to the difficulties encountered when reconstructing the geometry of three-dimensional complex microstructures, particularly when different phases are involved. This reconstruction step has to be implemented by users according to the microstructure of interest. In an attempt to reach the non-linear response of a soft matrix filled with rigid particles up to 55vol%, we have used the Abaqus mesh-to-mesh solution mapping exploring the pros and cons of such a process. Subsequently, exploiting the numerically-obtained non-linear response of the heterogeneous materials analyzed, we assess and further improve available analytical models existing in the literature. In particular, we propose explicit, albeit heuristic, extensions allowing to account for the percolation threshold of monodisperse sphere microstructures.

The paper is organized as follows. Section 2 presents the microstructure generation process as well as the FE simulations and illustrates the limited results obtained without remeshing. Then, Section 3 describes how remeshing and solution mapping are implemented and discusses at large the advantages and limitations of the technique. Section 4 focuses on the original results obtained for the case of quasi-rigid particles while Section 5 focuses on porous materials. In both of these sections, we introduce the newly obtained numerical homogenization results and discuss how the existing and newly proposed analytical models compare with the FE data. In Section 6, we conclude the paper.

2. Preliminaries

2.1. Microstructure generation

In this work, we focus on two-phase composites comprising monodisperse spherical particles distributed randomly and uniformly in an elastomer matrix. We construct numerically three-dimensional periodic unit-cells at various particle volume fractions c up to 0.55 following the process detailed in de Francqueville et al. (2019) (based on the work of Lubachevsky and Stillinger (1990)). In this construction, one may identify three parameters that have an impact upon the resulting mechanical properties: the volume fraction c, the number of inclusions N and the minimum distance between inclusions. We discuss those parameters in detail below.

Volume fraction c. The maximum theoretical volume fraction of inclusions that may be reached following the present procedure is limited to approximately 0.64, which stands for the *approximate* percolation threshold reported for both experiments and computations (Scott, 1960; Torquato and Stillinger, 2010). Inclusion clusters and percolation paths may enhance significantly the mechanical properties of such microstructures (Lefèvre and Lopez-Pamies, 2022), but may also introduce undesired anisotropy. In order to avoid inclusion percolation, the maximum volume fraction has been limited to $c = 0.55$ for which non-percolated microstructures are still reasonably easy to obtain, but also computations at finite strains can be carried out.

Number of particles N. For a large stiffness contrast between the matrix and the inclusions, such as a rubber matrix filled with silica particles, Gusev (2016) showed that 64 particles is a good compromise allowing to reach reasonably accurate and converging linear elastic (i.e. small strain) mechanical properties.[1] Yet, a special note is made

---

[1] Such a particle number should be taken with extreme caution when coupled properties such as magnetoelastic ones are sought. In such cases, this number may be substantially larger, e.g. 300–500 (Danas, 2017; Mukherjee et al., 2020, 2021). Nevertheless such properties are beyond the scope of the present study.

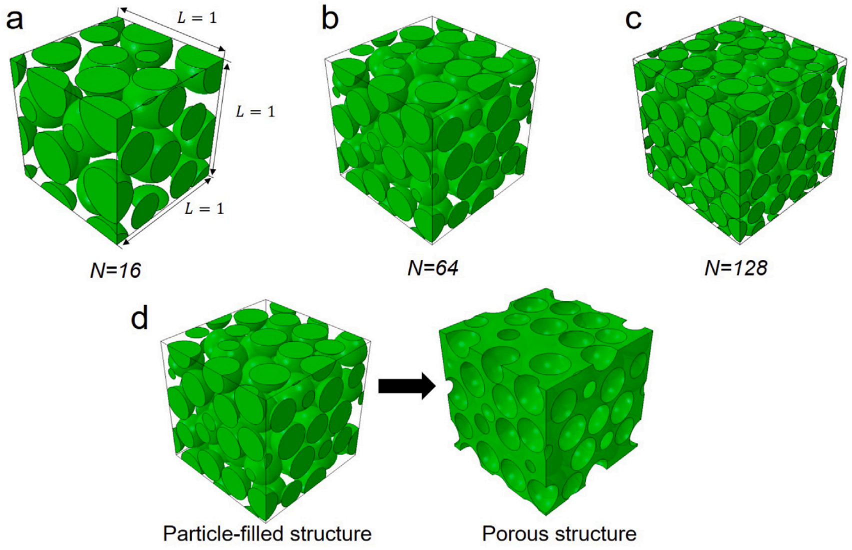

Fig. 2. (a)–(c) Different realizations of representative periodic cubic unit cells containing N randomly distributed monodisperse spherical inclusions for the same volume fraction $c = 0.55$. (d) Porous structure obtained from a particle filled microstructure by removal of the particles.

to the more recent study of Ghosh et al. (2023), where for a more converged linear elastic isotropic response a much larger number of particle may be required. In this study, we will try to reach the highest possible number of particles N that allows for a fairly converged (up to some dispersion) nonlinear elastic response and at the same time for computations to be carried out at reasonable computational cost and time, while reaching large overall strains.

Minimum distance between inclusions. For large volume fractions of inclusions, increasing the distance of particles leads to a smaller degree of clustering and thus to lower values for the elastic properties (Gusev, 2016). On the other hand, when this interparticle distance becomes too small, it may cause severe mesh distortion especially at finite strain FE simulations (Lopez-Pamies et al., 2013). Typically, for microstructures with low filler concentrations ($c < 0.3$), the minimum distance between inclusions lies between 1 and 10% of the particle diameter (Goudarzi et al., 2015; Guo et al., 2014; Jiménez, 2016). As the volume fraction c increases, the minimum distance decreases automatically. Furthermore, as the number of particles N increases the mesh size must decrease to maintain an accurate FE solution. In order to reach accurate modeling while still being able to run large deformation simulations, no minimum distance between inclusions is set *a priori* in our process but microstructures with interparticle distance less than 0.1% of the inclusion diameter are discarded *a posteriori*.

Since our focus is to obtain responses for large volume fraction of inclusions at finite strains, but also keep the computational cost at reasonable level, five realizations of 64 spheres each are built for volume fractions ranging between 0.38 and 0.55. Note that numerical studies for lower volume fractions have already been made in the literature (see for instance Lopez-Pamies et al., 2013) and thus will not be repeated here. In turn, the effect of the number of particles upon the converged response at finite strains is examined only for $c = 0.55$ by generating realizations with 16, 32, 64 and 128 inclusions (Fig. 2). Porous structures (Fig. 2d) are obtained from inclusion-filled microstructures by direct removal of the inclusion phase.

2.2. Meshing

Once a microstructure is generated, the first mesh is obtained by use of the open source Netgen (https://ngsolve.org) mesh generator (Schöberl, 1997; Gangl et al., 2020), which is particularly efficient in handling periodic boundary conditions. A ten-node tetrahedral quadratic element mesh is assembled with local refinement in areas where spheres are close to each other. For any FE simulation, and especially at finite strain, the mesh fineness constitutes a critical point. Coarse meshes produce inaccurate mechanical response, whereas an excessively refined mesh limits the simulation to extremely small strains. Therefore, in the present study, we choose to refine the meshes as much as this refinement does not become prohibitive for simulations at larger strains, while keeping a converged and accurate mechanical response. In the present work, we observe that for $N = 64$ and $c = 0.55$, a mesh with 1.2×10^6 degrees of freedom (which corresponds to approximately 3×10^5 elements) is a satisfactory compromise between convergence and problem size, as we will detail further below.

As discussed in the introduction, a large portion of the present work is dedicated to the use of a remeshing procedure allowing to increase the maximum strain attained by a direct finite strain simulation. Once the first mesh is generated with Netgen and the first simulation is conducted, the next remeshing steps are, in turn, achieved by use of the Gmsh (https://gmsh.info) open source mesh generator (Geuzaine and Remacle, 2009). The choice of NETGEN for the initial meshing is done because it allows to refine selectively the original mesh in thin matrix regions between closely packed particles. In turn, for remeshing, the choice of Gmsh is driven by its scripting language that proved to be more flexible to construct complex geometrical features. Specifically, the Gmsh code allows defining 3D complex objects by specifying a closed volume made up of a collection of planes (e.g., the element phases) without requiring the normals of the specified planes. As we will detail in Section 3, this feature facilitates the remeshing of complex geometries containing a large number of objects such as several inclusions. We close by noting that the present work focuses on spherical inclusions and *a priori* a simplified approach could have been used to read the deformed spherical particle shapes. Nonetheless, for the sake of generality and for potential use of such algorithms in more complex situations (e.g., deformable inclusions), a discrete reconstruction approach has been used, as will be discussed in detail Section 3.

2.3. FE simulations: material properties and boundary conditions

Both the nonlinear elastomer matrix (denoted with a subscript m) and particle (denoted with a subscript p) behaviors are described in the present work by a quasi-incompressible Neo-Hookean energy density (already implemented in Abaqus), as

$$\breve{W}_i(\breve{I}_1, \breve{J}) = \frac{\mu_i}{2}(\breve{J}^{-2/3}\breve{I}_1 - 3) + \frac{\kappa_i}{2}(\breve{J} - 1)^2, \qquad i = m, p \tag{1}$$

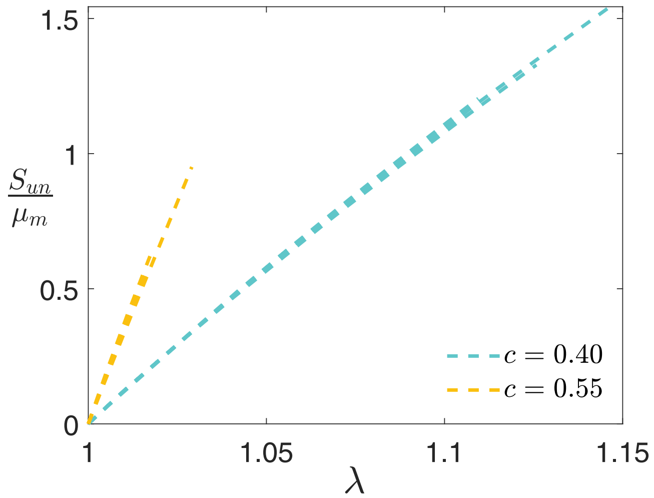

Fig. 3. Normalized macroscopic FE uniaxial tensile first Piola–Kirchhoff stress obtained for $N = 64$ particles and volume fractions $c = 0.4$ and 0.55 loaded along the three principal directions of the cubic cell.

where $\breve{I}_1 = \mathrm{Tr}(\breve{\mathbf{F}}^T\,\breve{\mathbf{F}})$ and $\breve{J} = \det \breve{\mathbf{F}}$, with $\breve{\mathbf{F}}(\mathbf{X})$ denoting the deformation gradient at the undeformed position $\mathbf{X}$.[2] The matrix material parameters μ_m and κ_m serve to denote the shear and bulk moduli, respectively. The bulk modulus is set to $\kappa_m = 10^4\,\mu_m$, which constitutes a representative value for rubber like material but also allows to obtain an overall response that is practically incompressible. Use of an infinite value (allowed by Abaqus) did not show any particular differences in the homogenized response. Instead, a finite value of κ_m has accelerated the simulations. In a similar fashion, the particles are considered quasi-rigid compared to the matrix. For numerical convergence, which requires a finite property contrast, we choose the particle shear modulus to be $\mu_p = 10^3\,\mu_m$ while $\kappa_p = \kappa_m$. Given that the resulting strains in the particle will be approximately zero, the value of κ_p has almost no effect in this case. Finally, the particle/matrix interface is assumed to be perfect (i.e. no debonding is considered). All of the above choices of parameters allow to obtain a practically incompressible homogenized response of the particle-matrix composite.

Subsequently, we consider periodic boundary conditions at the opposite faces of the cubic unit cell, while uniaxial tension or compression is applied in our simulations. Specifically, since the periodic boundary conditions correspond to linear constraints between nodes lying at opposite faces of the cube, we use the `*EQUATION` option to implement them. For a more detailed description of employing such boundary conditions, the reader is referred to Lopez-Pamies et al. (2013).

The FE simulations are carried out in Abaqus (2021) with hybrid quadratic tetrahedral elements, denoted `C3D10H`, allowing to deal with the quasi-incompressible behavior of the matrix phase. In addition, the `*NLGEOM` option is activated to account for finite strains.

Furthermore, we choose to work with the Abaqus implicit solver instead of the explicit one for various reasons. First, the `C3D10H` elements, which are appropriate for such complex microstructures, are only available with the Abaqus implicit solver. In turn, the explicit solver imposes the use of linear hybrid elements, such as `C3D4H`, which may provide accurate results in finite strains only via extremely refined meshes. Other elements may be used (such as hexahedral ones) but meshing the present microstructures properly becomes substantially more difficult. Second, the mesh-to-mesh solution mapping technique, which is the only remeshing technique recommended for hyperelastic materials in Abaqus, is not available with the Abaqus explicit solver. More importantly, we believe that in future works, the present implicit simulations may be used as reference results for assessing the convergence and accuracy of explicit simulations, which may reach larger strains and without remeshing but are often considered less robust or rigorous. The present simulations, reaching up to 1.2×10^6 of degrees of freedom, are performed on the Cholesky cluster of Ecole Polytechnique (https://meso-ipp.gitlab.labos.polytechnique.fr/user_doc/). Each simulation is run on 2 CPUs of 40 cores (Intel Xeon CPU Gold 6230 20 cores 2.1 GHz) and lasts between one and four hours of CPU time for 1% strain increments.

2.4. *Effective uniaxial stress–stretch response*

The effective response of the composite is analyzed in terms of the average first Piola–Kirchhoff stress, $\mathbf{S}$ and the average deformation gradient $\mathbf{F}$. In order to obtain those average quantities, we first define the average Cauchy stress (given by default in Abaqus calculations) by

$$\boldsymbol{\sigma} = \frac{1}{V}\int_V \breve{\boldsymbol{\sigma}}(\mathbf{x})dV. \tag{2}$$

Here, V and $\mathbf{x}$ denote the deformed volume of the unit cell and position vector, respectively. Subsequently, the average first Piola–Kirchhoff stress, $\mathbf{S}$ is defined by

$$\mathbf{S} = J\boldsymbol{\sigma}\mathbf{F}^{-T}, \qquad \mathbf{F} = \frac{1}{V_0}\int_{V_0} \breve{\mathbf{F}}(\mathbf{X})dV_0, \quad J = \det \mathbf{F}, \tag{3}$$

where $\mathbf{F}$ and $\mathbf{X}$ stand for the average deformation gradient of the composite and the reference position vector, respectively. Moreover, V_0 denotes the reference volume.

In the following, we apply a uniaxial tension loading along a given direction which corresponds to imposing one of the average diagonal components of $\mathbf{F}$, e.g. $F_{11} = \lambda$ (with λ denoting the average applied stretch) and then computing the corresponding axial component of $\mathbf{S}$, denoted henceforth as S_{un}. We also apply for the off-diagonal components $F_{ij} = 0$ with $i \neq j$ $(i, j = 1, 3)$, while the faces of the unit cell with normal $\mathbf{N} = \mathbf{e}_2$ and $\mathbf{N} = \mathbf{e}_3$ are (average) traction-free but still coupled via equations imposing periodicity of the displacement on opposite faces. This load ensures an overall uniaxial tension, up to some tolerance related to the isotropy of the unit cell, which, in turn, is related to the number of particles and the random process of placing them in the unit cell (Shrimali et al., 2020). We note further that the average uniaxial tension loading considered here is a special case of the more general stress triaxiality and Lode parameter load control discussed in the earlier studies of Barsoum and Faleskog (2007) and Mbiakop et al. (2015). Those approaches do not require any iterations to achieve an average stress state in the unit cell.

As a first illustration, Fig. 3 presents the first Piola–Kirchhoff stress–stretch uniaxial tension response in the three main cubic directions of microstructures comprising $N = 64$ particles with volume fraction $c = 0.40$ or $c = 0.55$. The superposition of the curves implies a cubic symmetry and together with the random distribution of the particles and realization analysis (presented in the following sections), one may infer a fairly converged isotropy of the unit cell, again up to some acceptable tolerance and scatter. The quasi-incompressible response of the unit cell may further be verified by evaluating the average determinant of the deformation gradient, which is found to remain $J \approx 1$. We note that the maximum numerically-attainable stretch decreases significantly with increasing volume fraction, as intuitively expected. For $c = 0.40$, the maximum stretch reaches a maximum value of $\lambda \simeq 1.15$ while this value drops to only $\lambda \simeq 1.02$ for $c = 0.55$. This is a mere consequence of the increasingly high packing of the particles and is attributed to the excessive element distortion caused by very large local strains, even at small macroscopic stretches. To exhibit this large strain concentration, we investigate the most unfavorable simulation among those studied in the present study, corresponding to a unit cell

---

[2] We note at this point that the superscript $\breve{(\cdot)}$ is used to denote local quantities, while the corresponding average ones will have no particular notation.

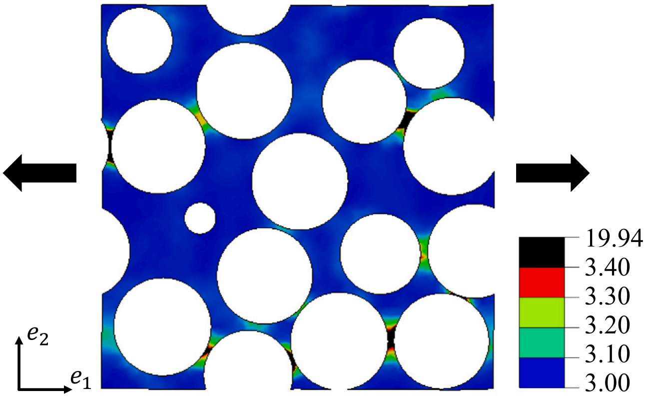

Fig. 4. Cross-sectional contour of the local strain invariant $I_1(\boldsymbol{x})$ recorded at a macroscopic strain invariant value $I_1 = 3.0009$ for a $N = 64$ particles and $c = 0.55$ microstructure. Black arrows indicate the uniaxial tensile loading direction. The particles are shown in white to improve visualization of the local fields.

comprising $N = 64$ and $c = 0.55$. Specifically, Fig. 4 shows a cross-sectional representative contour map of the local invariant $\check{I}_1$ with the particles removed to enhance the visualization of their position. It can be observed that the maximum values are mainly located in the regions between particles where the inter-particle distance is small. For instance, we observe a local maximum value of $\check{I}_1 = 19.94$, which is more than 6 times its average value $I_1 = 3.0009$. The latter remains almost unchanged compared to its initial value of $I_1 = 3$. This indicates that extremely large local deformation occurs at various positions even at very small overall macroscopic stretches, especially at such large particle volume fractions, and explains the severe mesh distortion, which in turn lead to failure of the simulation. Therefore, at such large volume fractions and without any remeshing procedure, simulations terminate at uninteresting small macroscopic strains and the nonlinear response of the composite cannot be assessed. In order to remedy this problem, we use next the `*MAP SOLUTION` option provided by Abaqus. This option together with custom-made remeshing scripts (which are presented below) allows us to enhance the macroscopic stretch that one may reach in such complex finite strain problems.

3. Remeshing and mesh-to-mesh solution mapping technique

One option to push forward the simulations at large strains is to include remeshing steps, which allows to improve the mesh quality and continue to strain the material locally. When dealing with hyperelastic materials, the only option provided by the Abaqus implicit solver is the mesh-to-mesh solution mapping technique. This section provides an overview of the technical aspects of the procedure as well as an example illustrating the performance and limitations of the method.

3.1. Procedure of the mesh-to-mesh solution mapping technique

Mesh-to-mesh solution mapping allows the transport of the stress and energy (but not strain) fields from a deformed mesh to a new mesh generated on the deformed structure with improved quality. This Abaqus built-in procedure involves the following steps,

Step 1. Run a FE simulation from a quality mesh.
Step 2. Extract the deformed mesh from the simulation. The deformed mesh is now also known as ‘orphan mesh’.
Step 3. Reconstruct the deformed geometry using the extracted deformed mesh.
Step 4. Generate a new mesh with improved quality on the deformed geometry.
Step 5. Map the solution from the orphan mesh to the new mesh using techniques such as interpolation or projection.

In practice, every step, excluding Steps 3 and 4, is carried out directly in Abaqus. In turn, the highly non-trivial Steps 3 and 4 have to be developed by users and should be adjusted to the geometry of interest. In the present work, Step 3 has been implemented writing a Python script that reconstructs geometries based on the identification and connection of element surfaces on the unit cell boundaries and/or the inclusion/matrix interfaces. A general methodology to identify surfaces consisting of connected or disconnected (such as in mesh-free simulations Kumar et al., 2019) nodes in a given geometry is described in detail in Appendix. Another simpler option, of course, consists in using the existing mesh connectivity of the original mesh to recover the new deformed surfaces. Nevertheless, this part of the code is extremely fast even using the more general option and thus is retained here. The resulting geometries are then remeshed using the open source mesh generator Gmsh. It is important to note at this point that the remeshing procedure can be used as many times as this is necessary to allow larger overall deformation of the unit cell. Usually, this requires a brute force trial and error approach as will be discussed below, since the number of remeshing steps is highly dependent on the volume fraction c as well as sometimes on the realization itself. Rule of thumb suggestions will be provided in the following.

3.2. Solution mapping and equilibrium check

In order to map the solution from the orphan deformed mesh to the new mesh, Abaqus provides the `*MAP SOLUTION` option using extrapolation and interpolation. This process consists mainly of three steps: (1) extrapolation of field variables (stresses, elastic energy, temperature, plastic strain...), from integration points to nodes of the original mesh, (2) import of a new mesh with new integration points and (3) for each new integration point, the stress and energy field variables are assigned by identifying in which element of the old mesh the point is located and by interpolation of the variable with the values at the identified element nodes. Note that the elastic strain and displacement fields are not transferred and are reset to zero in the following simulation considering the new mesh as undeformed.

After mapping the aforementioned field variables at the integration points of the new mesh, an initial step to check mechanical equilibrium and resolve stress unbalance is advised. In this step, no additional load is applied, whereby the Dirichlet boundary conditions, which are not transferred from the orphan mesh, should be set equal to those in effect before the remeshing. After equilibrium is achieved in this intermediate step, the analysis can be resumed with the application of the boundary conditions of interest. It may occur that achieving stress equilibrium is difficult, taking too long or even failing to converge. This is simply a consequence of the FE interpolation and extrapolation process from the orphan to the new mesh, which leads to stress fields that are not exactly the same in two meshes. In such a case, numerical damping may be used to facilitate the convergence with the option `*STATIC, STABILIZE, FACTOR=`*`damping`*. Ideally, one would like to keep the damping value as small as possible to minimize artificial microstructural changes. However, in practice, the damping value usually needs to be large in order to avoid fictitious instabilities due to abrupt (due to the remeshing) particle motions and thus achieve convergence of the stress equilibrium in the new mesh. Provided that the local mesh is not highly distorted, this process does not affect the actual solution significantly, and only helps to reach equilibrium in the new mesh with minor damped rearrangements of the particles as discussed next by use of an example.

Specifically, the solution mapping procedure and the use of numerical damping may introduce differences between the field variables in the old solution and in the new equilibrium solution, mainly in two ways. First, at the microscopic local scale, we note that the presented

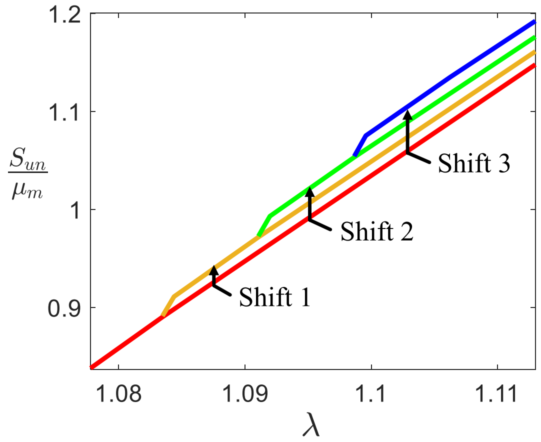

Fig. 5. Illustration of possible average stress jumps induced by the successive remeshings when parameters at hand are not carefully chosen.

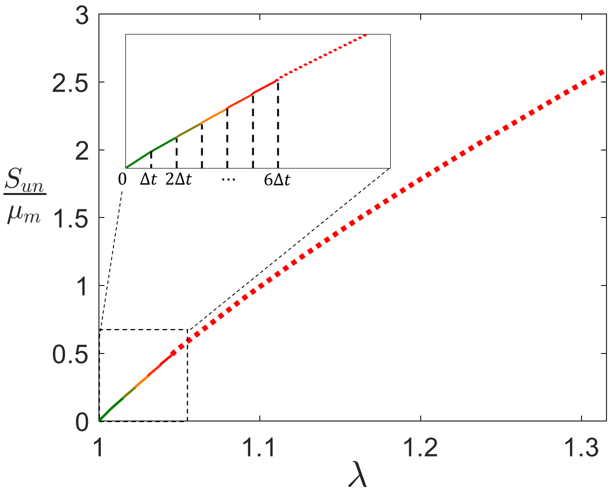

Fig. 6. Macroscopic stress–stretch uniaxial responses of a microstructure with $N = 64$ and $c = 0.4$ obtained by 6 remeshing steps.

technique is not entirely suitable for extracting exact local stress values in high-stress/strain concentration regions since the stress/strain gradients are smoothed by the remeshing. Second, at the macroscocpic average scale, depending on factors such as the time increment of remeshing, the number of distorted elements, and the level of mesh refinement, a jump in the average stress or strain energy may occur when restarting the calculations with the new mesh. These jumps are a direct consequence of minor rearrangements of particles locally. It is worth noting that if one considers a single particle geometry such stress jumps are not observed since interactions are non-existent or just invisible in this case. These jumps may accumulate with the successive remeshing operations leading to significant errors as illustrated in Fig. 5 sketching the average macroscopic stress possible shifts after remeshing during a uniaxial tensile loading. This implies that a large number remeshing attempts may lead in fact to less accurate results.

Keeping in mind these limitations, the next section demonstrates the relevance of the present procedure for determining the macroscopic stress–stretch response of a heterogeneous representative volume element, as long as the successive meshes are fine enough and the number of remeshing attempts is reasonable.

3.3. Size and number of remeshing steps

Determining the appropriate deformation increment for remeshing is a challenging task. According to the Abaqus documentation, it is recommended to perform remeshing at an early stage, in order to prevent excessive element distortion. If remeshing is delayed and several elements become distorted, it can lead to solution discontinuities and cause the simulation failure at the subsequent step of solution mapping. In addition, the corresponding deformation increment size (denoted as Δt) depends on the studied microstructure and most specifically on the maximum local deformation reached. For the microstructures of interest, we found that it depends strongly on the volume fraction c and the number N of inclusions. As any of these two quantities increase, it becomes necessary to decrease the increment size. To determine the proper increment size, a first simulation is run until reaching failure at t_{max}. Then, a remeshing procedure is tested with a relatively small increment size, $\Delta t \approx t_{max}/10$. If convergence cannot be achieved in the equilibrium check step, the increment size Δt is decreased until a suitable value is found. For instance, for a microstructure containing 64 inclusions with a volume fraction of $c = 0.4$ subjected to a uniaxial tensile loading, the first remeshing is made at stretch $\lambda = 1.01$. This strategy results to a maximum stretch at convergence failure of $\lambda \approx 1.32$ after six remeshing operations throughout the process, instead of $\lambda = 1.15$ without remeshing. This allows to reach an average strain that is almost two-and-a-half times larger than that obtained by a direct simulation.

Fig. 6 shows the macroscopic stress–stretch response of a microstructure ($N = 64$ and $c = 0.4$) obtained after 6 remeshing steps. One may notice in the inset of this figure the negligible jumps in the macroscopic average uniaxial stress along the successive remeshings. Moreover, these jumps are much smaller than the possible scatter resulting by the different realizations as discussed in the following section.

We finally note that the number of remeshing steps is limited for several reasons. First, the cumulative error may increase with the number of remeshing steps. Second, the remeshing procedure may be stopped by computational divergence during the equilibrium check step. Third, it may also become non-convergent by the extreme local deformation. In our case, at large volume fractions, neighboring spheres may come so close that a new satisfactory mesh is simply impossible to generate. Finally, the maximum overall stretch reached does not increase monotonously with the number of remeshing steps. It is observed for some microstructures, that while up to 13 remeshing steps were possible, generally the larger maximum stretch was obtained for a number of remeshing steps between 2 and 6. Thus, as a rule of thumb for the microstructures analyzed in the present work, we propose that the remeshing steps should not exceed the number of 6–7. Within this range, one obtains an acceptable compromise between accumulated errors, large macroscopic deformations and compute time.

4. Nonlinear behavior of particle-filled neo-Hookean composites

In the following, we focus on neo-Hookean matrix phases comprising quasi-rigid particles with volume fractions ranging from $c = 0.38–0.54$. We recall that the material parameters of the constitutive phases have been given in Section 2.3. The procedure presented here can be used directly for any other nonlinear elastic law from Abaqus material library. For instance, it was tested without additional difficulty on the Ogden's law.

4.1. Finite element estimates

In the previous section, we have described by means of representative examples the process of remeshing and stress mapping between different meshes during the deformation process. In this section, we use this flowchart to a large number of realizations, different number of particles and volume fractions to obtain numerical data for the

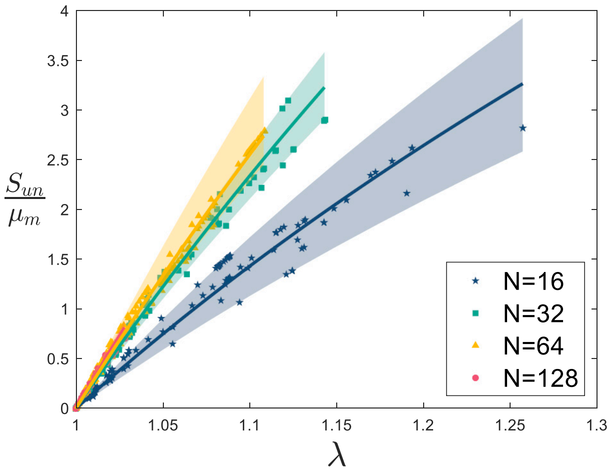

Fig. 7. Nonlinear uniaxial tensile stress–stretch responses for several microstructures with the same volume fraction $c \approx 54\%$ and different numbers of monodisperse spheres N.

average first Piola–Kirchhoff versus stretch response under uniaxial tension. In particular, by assessment of data dispersion, we decide on the best combination between number of particles per realization N and number of realizations that leads to a representative response of such composites. Those data will be then used in the next section to propose analytical models.

Specifically, several microstructures have been generated with $N =$ 16, 32, 64 and 128 spherical particles. Note that each microstructure can be subjected to uniaxial tensile tests at any of the three principal directions of the cube. Given the randomness of the microstructure, the three directions allow to assess at one hand the isotropy of the response and on the other hand, provide information on the realization scatter since each direction may be considered as a new data point. A total of ten simulations for each value of N have been performed.

Fig. 7 presents the scatter of the stress–stretch response obtained with remeshing for a volume fraction of $c = 0.54$. The continuous line displays an average neo-Hookean fit of all the data, while the scatter shadow shows the envelope containing every result obtained. As expected, the dispersion decreases with the increase of the number of particles N. Moreover, one notes that the effective response is globally underestimated for $N \leq 32$. It is thus important to mention at this point that performing a large ensemble averaging on realizations that are not sufficiently representative in volume, i.e., comprising a rather small number of particles (such as $N = 16$), may be extremely misleading and highly inaccurate in terms of average response, both at small (as is evident by the initial slopes) and large strains.

The average results for $N = 64$ and 128 particles appear to be very close to each other in the attained deformation range. However, the realizations containing $N = 128$ particles need substantially more refined meshes thus more computational resources while the maximum stretch reached is only $\lambda \approx 1.03$ despite the remeshing technique, while it is clear from the graph that the results for $N = 64$ may be considered sufficiently converged in the sense of average uniaxial tension response and relatively small scatter. It is worth noting that increase of N implies increase of the particle-matrix interfaces and thus of the regions of large strain and stress concentrations. Upon application of finite strains, particles tend to get in contact and such a situation leads fast to numerical divergence. A possible alternative to the process proposed here would be a meshfree approach as the one discussed in Kumar et al. (2019), but even therein contact of particles leads fast to numerical issues. In real situations, at such large local strains debonding and fracture may occur at the particle/matrix interface as discussed in de Francqueville et al. (2020), which leads to stress and strain relaxation and even opening of voids. Such simulations can then allow to reach larger strains but this is beyond the scope of the present work.

In conclusion, using $N = 64$ spheres seems to be the best compromise to obtain sufficiently accurate stress–stretch responses at large enough stretches to characterize the average nonlinear behavior of the material under consideration. Furthermore, as is evident in Fig. 7, several realizations are still required to reach a converged, average stress–stretch response. We emphasize, however, that convergence in this study is achieved by comparing the average response between $N = 64$ and $N = 128$, since a mere increase of realizations and lower particle number may lead to substantially softer results as is the case for $N = 32$.

In order to study the impact of the amount of fillers on the nonlinear behavior, additional microstructures with $N = 64$ particles and volume fractions of $c = 0.38$ and $c = 0.48$ have been generated to supplement those for $c = 0.54$. Fig. 8 reports data that have been obtained after simulating at least six realizations for each of the above-mentioned volume fractions. The results of these simulations provide the required data to assess the existing analytical models from the literature at high volume fraction, as well as to guide new more accurate ones.

In fact, one may easily recognize that the numerically-obtained nonlinear stress–stretch response follows to a very good approximation the equation

$$S_{un} = \mu(\lambda - \lambda^{-2}) \tag{4}$$

which implies an almost linear dependence of the energy function on the sole macroscopic I_1 invariant. In particular, this last equation is that corresponding to the uniaxial tension response of an incompressible neo-Hookean solid. Therefore, a direct fitted value of the effective μ can be obtained for a set of simulations corresponding to a given volume fraction in Fig. 8. It is noted here that the homogenized response of a two-dimensional composite comprising rigid inclusions embedded in an incompressible neo-Hookean matrix is *exactly* neo-Hookean as well Lefèvre et al. (2022). Nevertheless, that is not *exactly* true in three-dimensions, as already shown in Lopez-Pamies et al. (2013); yet it remains an extremely good and simple approximation as shown in Fig. 8b at fairly large strains.

Remark 1. At this point it is important to emphasize that at such large volume fractions obtaining the initial shear modulus by calibrating a finite strain neo-Hookean model is more relevant but may also be somehow different than that extracted by a direct small strain analysis. The reason is directly related to the fact that at regions of closely packed particles the local strains become exceedingly large and thus depart from the framework of small strain elasticity even at very small macroscopic strains, as shown in Fig. 4. This leads to lower local stresses very early on when a finite strain framework is used contrary to a small strain one. Resolving those local stress fields with a finite strain or a small strain theory can thus lead to differences in the initial slope (see for instance corresponding linear results in de Francqueville et al. (2019)). Similar observations were also made in Tarantino et al. (2019) in the context of highly porous materials and comparison between actual experiments and linear elastic simulations. In a sense, the range of validity of a small strain analysis approached zero very quickly especially at large volume fraction of inclusions.

4.2. Analytical models

In this section, we use the previous finite strain numerical data to assess existing analytical models and propose new ones. Given that the overall macroscopic response of the previously analyzed composites is quasi-incompressible, we specialize the models in the present section to the fully incompressible case. This allows to simplify significantly the modeling approach, while remaining consistent and accurate with respect to the corresponding numerical data.

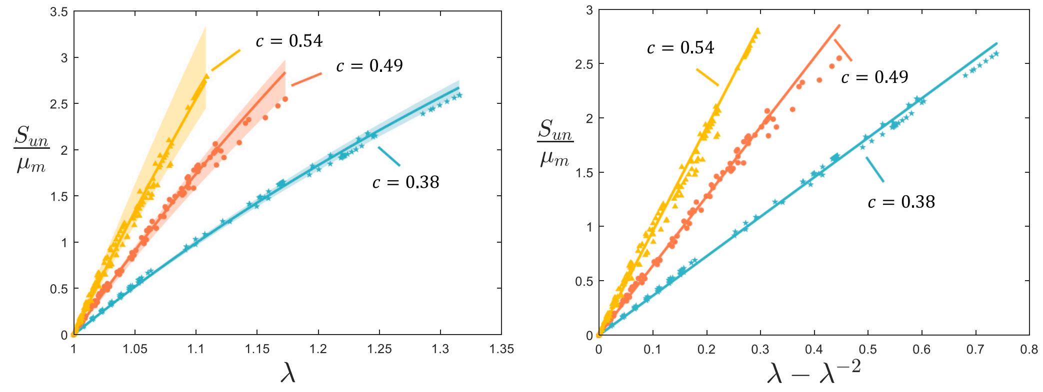

(a) (b)

Fig. 8. FE uniaxial tensile responses for $N = 64$ particles at different volume fractions, $c = 0.38, 0.48, 0.54$ showing the first Piola–Kirchhoff stress as a function of (a) the stretch λ and (b) $\lambda - \lambda^{-2}$ to reveal the neo-Hookean form of the response.

In the context of Fig. 8, we established that the effective response of a neo-Hookean matrix comprising large volume fractions of quasi-rigid particles distributed isotropically and uniformly remains to a fair extent also neo-Hookean and thus is described *entirely* by the effective shear modulus μ. The latter is a function of the particle volume fraction c and the matrix shear modulus μ_m. This result confirms and extends the previous finite strain studies in 2D (Lefèvre et al., 2022) and 3D (at smaller particle volume fractions $c < 0.3$) (Lopez-Pamies et al., 2013).

Following closely the existing literature on *incompressible* composites and considering first the case of linear elasticity, several analytical forms of the effective shear modulus μ may be obtained according to the chosen homogenization model. We present several of them in the present case and we identify one that allows the best fit all the way up to large particle volume fractions and monodisperse sizes.

The first exact solution for particle reinforced linear incompressible media was given by Einstein (1906) in the case of dilute volume fraction of rigid particles ($c \to 0$), such that

$$\mu = \mu_m + \frac{5}{2}\mu_m c + \mathcal{O}(c^2). \tag{5}$$

Evidently this expression is not expected to be accurate for large volume fractions. Nevertheless, it provides an exact dilute result which should be attained by any model proposed for arbitrary volume fractions.

Another famous and important result is the Hashin and Shtrikman (HS) *lower bound*[3] (Hashin and Shtrikman, 1961, 1963), which reads

$$\mu = \frac{2+3c}{2(1-c)}\mu_m. \tag{6}$$

Again, this result is extremely useful since any proposed model for isotropic particle reinforced incompressible composites must satisfy this bound. It also predicts that $\mu \to \infty$ as $c \to 1$. Moreover, it is trivial to show that the bound (6) recovers the exact dilute result (5) as $c \to 0$. It is noted however, that by construction this model describes better a polydisperse particle microstructure. Evidently, this is not the case in the present study, which focuses on monodisperse spheres.

The differential model uses an iterative scheme where the properties of a dilute composite are used to generate the properties of successive composites with increasing particle volume fraction until reaching the targeted finite concentration. This estimate is geometric in nature and leads to an effective shear modulus described by (Bruggeman, 1935; Norris, 1985),

$$\mu = \frac{\mu_m}{(1-c)^{\frac{5}{2}}}. \tag{7}$$

This estimate satisfies both the lower HS bound and recovers the dilute estimate (5) as $c \to 0$. Nonetheless, as its name suggests, it is again an estimate that is expected to be more appropriate for polydisperse microstructures instead of monodisperse ones.

Finally, several numerical studies (Gusev, 2016; de Francqueville et al., 2019; Segurado and Llorca, 2002; Kari et al., 2007) have shown that the generalized self-consistent (GSC) implicit model (Christensen and Lo, 1979) (which, in fact, was shown to be a differential coated sphere (DCS) construction Avellaneda, 1987; Lefèvre and Lopez-Pamies, 2015) provides a reasonable approximation for composites with monodisperse spherical inclusions. Nonetheless, as explained in Remark 1, those former FE estimates were obtained within a linear elastic framework inducing higher stresses locally and thus leading to an overall higher shear modulus. In general, the GSC model induces a special form of interactions, i.e. that of a coated sphere, and thus is expected to be less appropriate for the present monodisperse microstructures at finite strain since it exhibits a percolation threshold at $c = 1$ similar to the previously mentioned models.

More recently, in the context of linear elasticity and a complete range of particle volume fractions ($c = 0 - 1$), an explicit formula with two fitting parameters α_n and β_n ($n = 2$ for 2D and $n = 3$ for 3D) has been proposed by Lefèvre and Lopez-Pamies (2022), which reads

$$\mu = \frac{\mu_m}{\left[\left(1+\alpha_n\left(\beta_n+\left(\frac{c}{p_n}\right)^2\right)\left(\frac{c}{p_n}\right)^2\right)\left(1-\frac{c}{p_n}\right)\right]^{\frac{5p_n}{2}}}. \tag{8}$$

Here, p_n is the percolation threshold and acts as a given geometrical parameter if known *a priori*. For 3D spherical monodisperse inclusions, for instance, $p_3 \approx 0.64$. This model can be viewed as a generalization of the classical differential-scheme Eq. (7) at large volume fractions but as stated by the authors it can deal with monodisperse microstructures owing mainly to the presence of the percolation threshold parameter p_n. As an example, an infinitely polydisperse distribution of particles leads to percolation at $c = 1$, i.e., $p_3 = 1$ (see for instance Tarantino et al., 2019). In turn, monodisperse spherical particles have a much lower percolation threshold.

By setting $\alpha_3 = 1$, $\beta_3 = 0$ and $p_3 = 0.64$ in (8), we obtain a very accurate fit of the numerical values μ/μ_m extracted from Fig. 8 and shown in Fig. 9. The simpler estimate used here thus becomes

$$\mu = \frac{\mu_m}{\left[\left(1+\left(\frac{c}{p_3}\right)^4\right)\left(1-\frac{c}{p_3}\right)\right]^{\frac{5p_3}{2}}}, \qquad p_3 = 0.64. \tag{9}$$

By construction, the above equation satisfies the dilute result (5) as $c \to 0$, lies above the lower HS bound for all $c \in [0, p_3]$ and goes to infinity at $c = p_3 = 0.64$, which corresponds to the approximate percolation threshold of monodisperse spheres (Torquato and Stillinger, 2010). As

---

[3] The corresponding upper bound is infinite in this case of rigid particles.

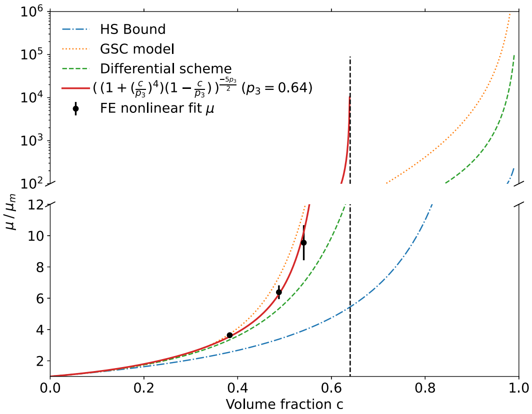

Fig. 9. Comparison between FE results extracted from Fig. 8 and analytical models for the composite normalized shear modulus as a function of the particle volume fraction.

shown in Fig. 9, Eq. (9) reproduces extremely well the corresponding numerical data for all volume fractions considered here and thus is able by extension to recover also the nonlinear response in Fig. 8. It is noted that the present model may be extended readily to non-Gaussian matrix phases following the nonlinear comparison composite approach used in Lopez-Pamies et al. (2013).

Remark 2. The model presented in Eq. (9) lies between the solutions of the GSC model and the differential scheme model. Interestingly, the difference between the GSC model and the differential scheme becomes larger with increasing volume fraction. While the GSC model (Christensen and Lo, 1979) is realized via a differential coated sphere microstructure (Avellaneda, 1987), the differential scheme corresponds to polydisperse microstructures where the particles have infinitely many sizes. Therefore, this difference between two analytical models can be directly linked to the influence of the distribution of the microscopic sizes (polydispersity). While it was reported that the polydispersity has no significant influence when $c < 0.30$ (see Lopez-Pamies et al. (2013) for particles and Zerhouni et al. (2019) for voids), instead monodisperse spherical particle-filled composites tend to be much stiffer than the polydisperse ones when $c \geq 0.35$. These observations are thus in agreement with the present results that show that the monodisperse FE results are stiffer than the differential-scheme results. Note, however, that there exist so many different microstructures that are mono- (Travers et al., 1987; Willot and Jeulin, 2009; Anoukou et al., 2018; Tarantino et al., 2016; Tarantino and Mortensen, 2022), bi- (Pickering et al., 2016; Bele and Deshpande, 2015; Bele et al., 2017) and polydisperse (Zerhouni et al., 2021; Neumann et al., 2020; Hooshmand-Ahoor et al., 2022) with very different responses that none of the classical models may properly model. In this regard, the versatile expression shown in Eq. (8) might allow for a wide range of modeling flexibility by calibration with available numerical or experimental data.

5. Nonlinear behavior of porous neo-Hookean materials

In this section, we provide numerical results and analytical models for the exactly opposite case of isotropic porous microstructures. The high-porosity unit cells are obtained by simply removing the particles from the previously generated geometries. The matrix phase follows exactly the same quasi-incompressible neo-Hookean law introduced in Eq. (1).

Contrary to the particle-filled composites, obtaining numerical results at large deformations is easier in the case of voids and requires in all cases considered here *no remeshing*. In turn, the obtained response is compressible and thus more complex, requiring more loading conditions to assess more thoroughly their behavior. We note here that the purpose of this section is not to study in the most complete manner the response of such porous materials, since they would require several different loading conditions with different stress triaxialities (see for instance Mbiakop et al., 2015; Shrimali et al., 2019). Instead, we are interested to merely explore the uniaxial, equi-biaxial and purely hydrostatic tension response of such composites and assess and improve the relevant existing analytical models at such high porosities.

5.1. Effective shear and bulk moduli

Fig. 10 shows a plot of our present FE results on several numerical realizations along with previous FE data at lower volume fractions of pores and several bounds and models. The following expressions are valid for an incompressible matrix phase (i.e., $\kappa_m \to \infty$) and zero moduli for the porous phase.

The first exact solution was given by Eshelby (1957) in the case of dilute volume fraction of a single void in an infinite matrix ($c \to 0$) as

$$\mu = \mu_m - \frac{5}{3}\mu_m c + \mathcal{O}(c^2), \qquad \kappa^{-1} = \frac{3c}{4}\mu_m + \mathcal{O}(c^2), \tag{10}$$

Note that due to the incompressibility of the matrix, at $c \to 0$ the result for κ is as expected singular. Again this expression is not expected to be appropriate for large porosities, however, it provides an exact dilute result that needs to be recovered by any model proposed for arbitrary porosities.

The Hashin–Shtrikman (HS) upper bound,[4] for isotropic porous materials reads

$$\mu_{HS} = \frac{3(1-c)}{3+2c}\mu_m \qquad \text{and} \qquad \kappa_{HS} = \frac{4(1-c)}{3c}\mu_m. \tag{11}$$

The solution of a differential hollow sphere assemblage, denoted here with "DA", shares the same expression for κ as the HS bound but leads to a shear modulus μ that reads (Shrimali et al., 2019; Lefèvre and Lopez-Pamies, 2014)

$$\mu_{DA} = \mu_m\left(1 - \frac{70c}{Z}\right), \qquad \kappa_{DA} = \kappa_{HS} \tag{12}$$

with

$$Z = 21 + 30c + 19c^{10/3} + (361c^{20/3} + 76c^{13/3} - 5502c^{10/3} + 9408c^{8/3} - 4700c^2 - 84c + 441)^{1/2}.$$

Finally, we also include for completeness the finite-percolation Budiansky-Hill model (Budiansky, 1965), which takes the form

$$\mu = \frac{3(1-2c)}{3-c}\mu_m \text{ and } \kappa = \frac{4(1-2c)(1-c)}{(3-c)c}\mu_m. \tag{13}$$

We note that all finite porosity models described above recover the dilute results of Eshelby in (10) and satisfy the HS bound (11).

We observe in Fig. 10 that the DA model reproduces extremely well the FE results for both the effective shear and bulk moduli. Nevertheless, it is noted that it leads to $\mu = \kappa = 0$ at $c = 1$, contrary to the present monodisperse unit cells, which lead to percolation and thus zero effective stiffness at $c = 0.64$. On the other hand, the Budiansky-Hill model underestimates significantly both moduli but in turn contains a percolation limit at $c = 0.5$.

In order to remedy this point, we propose, similar to the particle case, a modification of the DA model to include percolation effects at finite porosities. To achieve this, we introduce first a sigmoid-type function of the volume fraction of the form

$$g_a(c; a, p_3) = \frac{a(p_3 - c)}{\sqrt{c^2 + a^2(p_3 - c)^2}}, \quad c \in [0, 1], \quad p_3 \in [c, 1], \quad a \geq 0. \tag{14}$$

In this expression, p_3 serves again as the volume fraction at which percolation is reached, whereas a controls how fast or slow this function will affect the corresponding moduli. Moreover, as $c \to 0$, $g = 1 - \mathcal{O}(c^2)$, which implies that multiplication of any of the moduli with g does

---

[4] The lower bound is zero in the porous case.

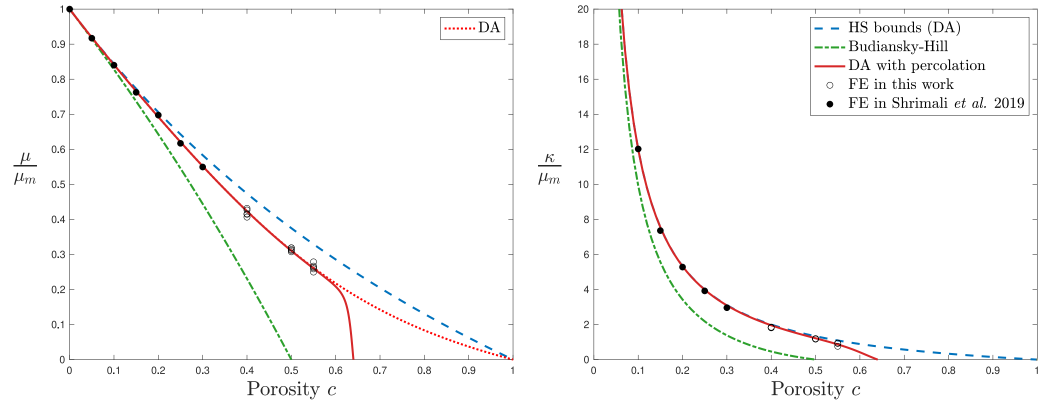

(a) (b)

Fig. 10. Comparison between FE linear elastic properties for porous microstructures and existing analytical models. Normalized (a) shear modulus μ/μ_m and (b) bulk modulus κ/μ_m as a function of porosity c.

not alter their ability to recover the dilute result (10). Using thus the function g in Eq. (14) and the same percolation threshold with the particles, $p_3 = 0.64$, one may re-write the previous DA estimates as

$$\mu_{DAp} = g(c; 50, 0.64)\,\mu_{DA}, \qquad \kappa_{DAp} = g(c; 8, 0.64)\,\kappa_{DA}. \tag{15}$$

We note that the use of different values of a for the shear and the bulk moduli is motivated by corresponding data at large strains to be discussed in the following section.

5.2. Nonlinear hyperelastic behavior

In this section, we discuss the nonlinear response of the porous materials submitted to finite strain tensile tests. Contrary to the simple response obtained for particle composites, porous materials made of an incompressible matrix exhibit an overall compressible behavior. Furthermore, at finite strains, the dependence of the energy density on the average deformation gradient is highly non-trivial. In order to reveal this dependence, we choose to work with three loading conditions: (i) uniaxial tension with $\lambda_1 = \lambda$, (ii) equi-biaxial straining with $\lambda_1 = \lambda_2 = \lambda$ and (iii) purely hydrostatic tension with $\lambda_1 = \lambda_2 = \lambda_3 = \lambda$. In all cases, the off-diagonal components of $\mathbf{F}$ are set equal to zero whereas in the first two cases (i) and (ii) the remaining normal average stresses are set equal to zero, respectively.

We present in the following two finite strain analytical models. The principal one is that proposed by Shrimali et al. (2019), which takes the form

$$W(\mathbf{F}, c) = \frac{3(1-c)\,\mu_m}{2(3+2c)}\left[I_1 - 3\right] + \frac{3\mu_m}{2J^{1/3}}\left[2J - 1 - \frac{(1-c)\,J^{1/3}\left(3J^{2/3} + 2f_0\right)}{3+2c} - \frac{c^{1/3}J^{1/3}\,(2J+c-2)}{(J-1+c)^{1/3}}\right]. \tag{16}$$

The resulting average stress becomes

$$\mathbf{S}(\mathbf{F}) = \frac{\partial W}{\partial \mathbf{F}} = \frac{3(1-c)\,\mu_m}{3+2c}\mathbf{F} + \frac{\mu_m}{2}\left[\frac{3+6J+2c(1+7J)}{(3+2c)\,J^{1/3}} + \frac{c^{1/3}J\,(4-5c-4J)}{(J+c-1)^{4/3}}\right]\mathbf{F}^{-T}. \tag{17}$$

This model has certain important features that are discussed in detail by the authors in their work. We summarize below the main ones.

- At small strains, the model (16) leads to the HS estimates (11). Thus, by construction, it overestimates the shear modulus predicted by the FE simulations (see Fig. 10).
- For isotropic deformations (e.g., purely hydrostatic tension) and a neo-Hookean matrix phase, (16) agrees exactly with the results of Hashin (1985) for a composite sphere assemblage microstructure.
- The model (16) is of a separable form in terms of the invariants I_1 and J.
- The model allows to model also non-Gaussian matrices.

Following closely the Shrimali et al. model presented previously, we propose a few modifications that allow to have a finite percolation threshold response, while recovering the DA estimates presented in the previous section at small strains. At the same time, we try to retain the main features of the previous model. We thus propose the following energy function

$$W(\mathbf{F}, c) = \mu_\infty I_1 + A I_1^q + B + \frac{3\mu_m}{2J^{1/3}}\left[C(2J-1) - D\frac{(1-c)\,J^{1/3}\left(3J^{2/3} + 2f_0\right)}{3+2c} - E\frac{c^{1/3}J^{1/3}\,(2J+c-2)}{(J-1+c)^{1/3}}\right]. \tag{18}$$

The corresponding first Piola–Kirchhoff stress is then given by

$$\mathbf{S}(\mathbf{F}) = 2\left(\mu_\infty + A q I_1^{q-1}\right)\mathbf{F} + \frac{\mu_m}{2}\left[C\frac{(4J+1)}{J^{1/3}} + D\frac{6(c-1)J}{(3+2c)J^{1/3}} + E\frac{c^{1/3}J\,(4-5c-4J)}{(J+c-1)^{4/3}}\right]\mathbf{F}^{-T}. \tag{19}$$

Expressions of the unknown parameters $A-E$ are obtained by imposing that the proposed finite strain model linearizes to the corresponding DA estimates while leading to the desired slopes at very large strains. Note that the constant B is simply used to lead to a zero energy density for $\mathbf{F} = \mathbf{I}$. With that in mind, we find

$$A = \frac{3^{1-q}(\mu_{DAp} - 2\mu_\infty)}{2q}$$

$$B = -\frac{3(\mu_{DAp} + 2\mu_\infty(q-1))}{2q}$$

$$C = \frac{\left(-10c^2 + c + 24\right)\mu_{DAp} - 3c(4c+15)\kappa_{DAp}}{(c-1)(31c+36)}$$

$$D = \frac{(2c+3)((3c+8)\mu_{DAp} - (15c)\kappa_{DAp})}{(c-1)(31c+36)}$$

$$E = \frac{3c((2c+3)\mu_{DAp} - (10c+9)\kappa_{DAp})}{(c-1)(31c+36)}.$$

In these expressions, μ_{DAp} and κ_{DAp} correspond to the shear and bulk moduli, respectively, of the differential hollow sphere assemblage microstructure defined in (15). The modulus μ_∞ serves to describe the

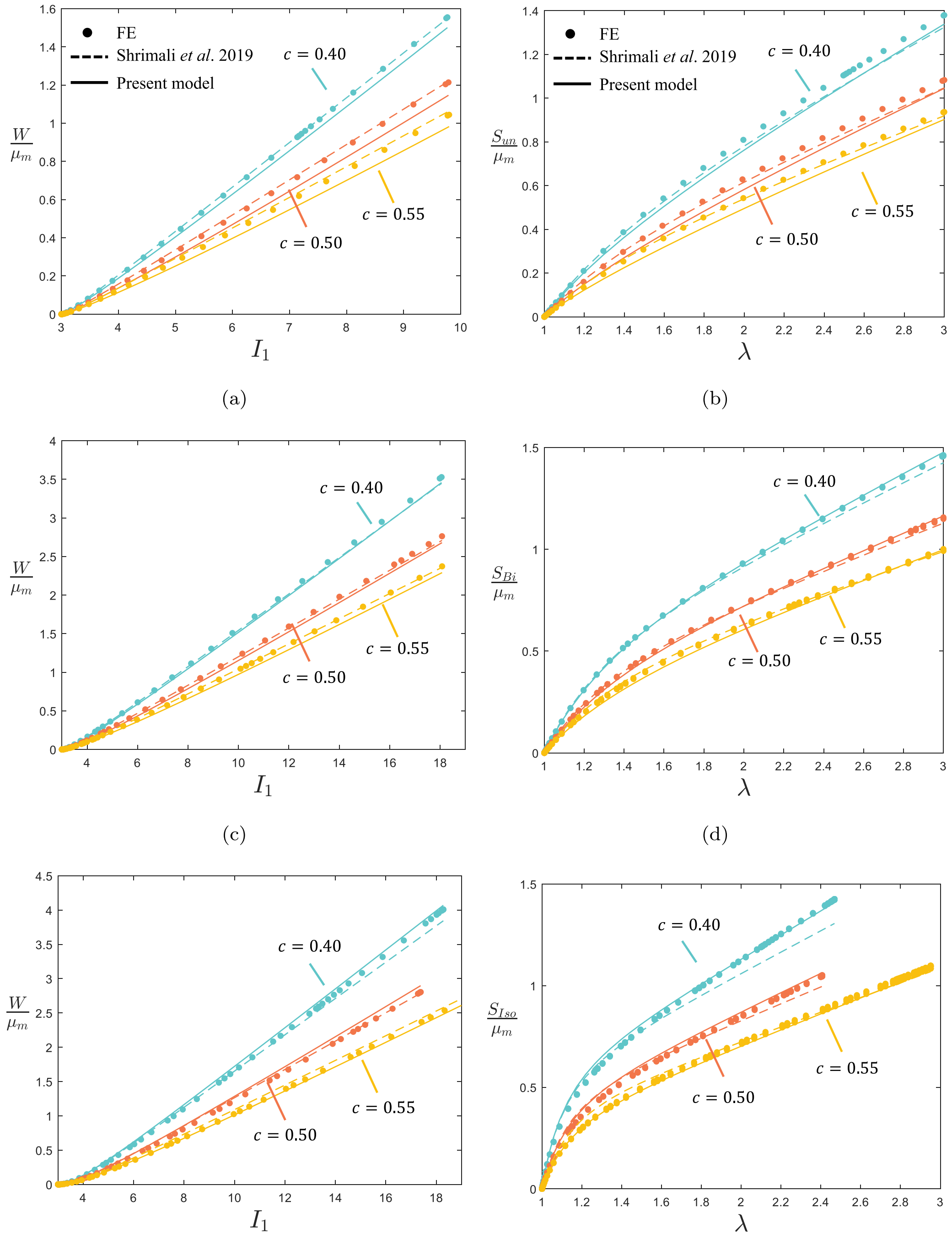

(a) (b)

(c) (d)

(e) (f)

Fig. 11. FE and model comparisons for the effective nonlinear elastic energy W/μ_m and the first Piola–Kirchhoff stress $\mathbf{S}/\mu_m$ for microstructures of initial porosities $c \in (0.4, 0.5, 0.55)$ submitted to (a-b) uniaxial tension, (c-d) equi-biaxial tension and (e-f) purely hydrostatic tension.

behavior of the energy function which is linear in I_1 at very large strains. Using Eq. (14) in Shrimali et al. (2019), we obtain

$$\mu_\infty = \frac{(1-c)\mu_m}{2+c}\, g(c; 50, 0.64).$$

Here, again the sigmoid function g defined in (14) has been used to comply with a finite percolation threshold. Finally, the value $q = 1/9$ is obtained by calibration with the finite strain numerical results.

It is noted here that extension of the newly proposed model to non-Gaussian matrices can be obtained by use of the nonlinear comparison approach discussed in Shrimali et al. (2019). Moreover, the proposed modification may allow to model by further calibration other types of porous materials with different microstructures such as the ones generated in Hooshmand-Ahoor et al. (2022).

In Fig. 11, the proposed models are assessed with corresponding FE simulations for three different loading conditions and three large initial porosities, $c = 0.4, 0.5, 0.55$. Only one realization has been plotted to illustrate the FE results, since they exhibit very small dispersion in the case of porous microstructures. Overall, both models described in the present study are in excellent agreement for all loads presented here. The estimates of the Shrimali et al. model are remarkably close to the FE results even for large monodisperse porosities despite the fact that it percolates at $c = 1$ and has been proposed mainly for polydisperse microstructures. In fact, we observe that the differences between the

HS and the DA models in linear elasticity are smeared out at large strains. By construction, the present proposed model (18) is also in very good agreement and in some cases performs slightly better while in others slightly worse than the one of Shrimali et al. The FE results confirm a linear dependence on I_1 at large strains and large porosities. Moreover, the difference between the analytical models and the FE simulations decreases with increasing initial porosity for $c \geq 0.40$. This is consistent with recent experimental and numerical results in linear elasticity (Zerhouni et al., 2019; Tarantino et al., 2019).

6. Conclusion

In the present study, we have proposed small and finite strain numerical homogenization results of a neo-Hookean elastic matrix comprising a large volume fraction of isotropically distributed, monodisperse spherical rigid particles or voids, up to a volume fraction of $c = 0.55$. This was achieved by successive remeshing together with the use of a solution mapping technique. This allowed us to obtain FE solutions with an implicit solver and more importantly to increase the macroscopic strains that may be attained numerically. For representativity of the results, several realizations were analyzed in different cubic directions, while a convergence analysis with respect to the total number of inclusions was carried out. We found that a number of $N = 64$ inclusions was a good compromise between obtaining sufficiently converged results and maximum CPU time and memory.

The obtained FE results allowed to propose homogenization-guided analytical models both for the case of rigid particles and voids. In both cases, we have observed the importance of including a percolation threshold, which is reached at $c \approx 0.64$ for monodisperse spherical inclusions. In particular, for rigid particles, the FE were found to lie between the differential and the generalized self-consistent (which is in fact equivalent to the differential coated sphere construction) schemes for values up to $c = 0.55$. However, both of these models exhibit a percolation at $c = 1$ and thus are incapable of capturing the response at volume fractions very close to percolation. For that reason, use of the heuristic linear model of Lefèvre and Lopez-Pamies (2022) was made to obtain a better fit of the FE results by proper calibration. In agreement with earlier studies at smaller volume fractions, the present FE also confirmed that the resulting homogenized response is also neo-Hookean, i.e., that of the matrix simply reinforced by the initial shear modulus at small strains. This allowed for a very simple modeling approach at large strains.

Subsequently, we have carried out equivalent FE simulations for porous materials by simple removal of the particle phase. For a better assessment and given that the response of the porous material was compressible, we have carried out simulations for three different loads with increasing triaxiality, i.e., uniaxial, equi-biaxial and purely hydrostatic tension. Remarkably, in the context of voided microstructures, no remeshing was required even up to strains as large as 200%. In this case of monodisperse spherical voids, we have found that the best model at small strains is that of the differential hollow sphere assemblage (DA) construction. For consistency with the previous particle case, we have also proposed a modification of the DA model to include a percolation threshold at a porosity of $c = 0.64$. At finite strains, we have compared the FE results with the model of Shrimali et al. (2019) and the agreement was found to be very good. This last model, however, leads to the Hashin–Shtrikman estimates at small strains and thus has a percolation at $c = 1$. For that reason, starting from this model, we have proposed a modified model that allows to recover the DA estimates at small strains, percolate at finite values of porosities and still remain as accurate as the Shrimali et al. model at finite strains and different loads with respect to the corresponding FE results.

We close by noting that the numerical methodology presented here is applicable to different types of composites, such as polydisperse spherical, ellipsoidal, or polyhedral particles, as well as particle-pore mixed structures with any combination of their volume fractions. Finally, it is perhaps relevant to mention that alternative numerical methods may allow to reach even larger overall strains in particle reinforced composites such as the mesh-free technique presented for instance in Kumar et al. (2019). Note, however, that those should be somehow extended to quasi-incompressible phases and more importantly be implemented in more general purpose software that would allow for easy use.

CRediT authorship contribution statement

H. Luo: Lead research investigator for development of methodology, programming and software development, F.E. simulations, Result analysis, Co-Lead in writing and manuscript preparation. **Z. Hooshmand-Ahoor:** Contributed significantly to software development, Contributed to result analysis and discussion, Manuscript reviewing. **K. Danas:** Initial formulation of research goals and aims, Provided initial code components, implementation and algorithm support, Results analysis and development evolution, model formulation, Writing and manuscript preparation. **J. Diani:** Initial formulation of research goals and aims, Provided initial code components, Results analysis and development evolution, Writing and manuscript preparation, Project administration, Acquisition of the financial support for the project leading to this publication.

Declaration of competing interest

The authors declare that they have no known competing financial interests or personal relationships that could have appeared to influence the work reported in this paper.

Data availability

Data will be made available on request.

Acknowledgments

The work benefited from the support of the Chair Modeling advanced polymers for innovative material solutions led by the Ecole polytechnique (l'X), France and the Fondation de l'Ecole Polytechnique, France and sponsored by Arkema, France. ZHA and KD acknowledge support from the European Research Council (ERC) under the European Union's Horizon 2020 research and innovation programme (Grant-No. 101081821).

Appendix. Details about the geometry reconstruction code

The main idea of the geometry reconstruction presented in Section 3 is to detect from the old mesh, all element faces at the particle/matrix interfaces, noted s_2, or on the cube surfaces, noted s_1 (Fig. A.12a), and connect them into closed volumes. The flowchart given in Fig. A.12b consists in five steps: (1) The old orphan mesh is imported with the essential information including the coordinates of the nodes and connectivity. (2) The set of element faces pertaining to the same closed surface s are identified and saved. (3) A set of all closed volumes defined by each surface s is constructed. (4) Finally, a Boolean difference between the largest volume (outer boundary) and the other volumes (inclusions) is performed to define the matrix and/or inclusions regions. (5) Final geometry is exported to generate a new mesh.

In order to achieve step (3) efficiently, we propose to reduce the loop process, by defining two map relations during step (2). The first one defines subsets of every point p belonging to each closed surface s. The second relation defines subsets of every element faces attached to a surface s. Actually, this procedure has been inspired from the region growing segmentation method where the growing criterion is the presence of common points.

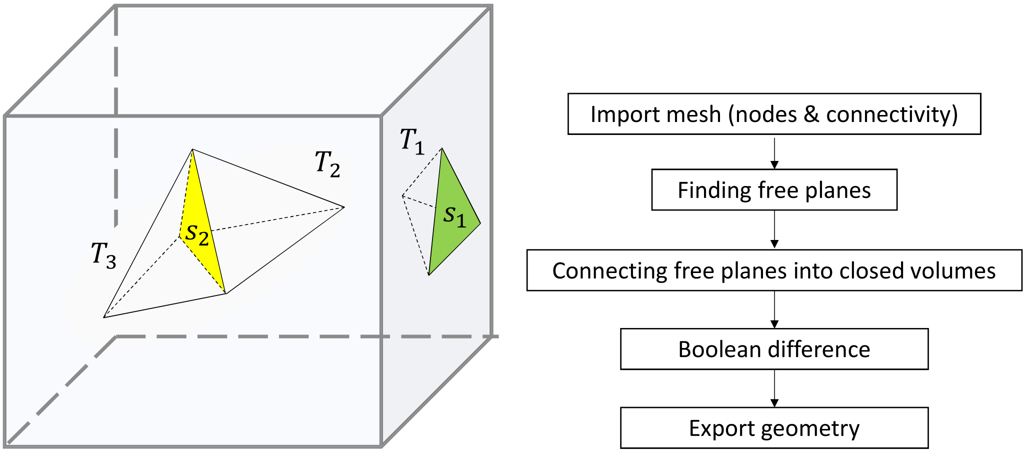

(a) (b)

Fig. A.12. (a) Illustration of the element faces of interest defining sets s_1 and s_2. Element faces from s_1 belong to one tetrahedral element T_1 only. Element faces of s_2 belong always to two elements T_2 and T_3 from the different phases. (b) Flowchart of the geometry reconstruction from a mesh. The exported geometry is then used to generate a high-quality new mesh.

References

Abaqus, 2021. SIMULIA Abaqus User Assistance. Simulia.

Anoukou, K., Brenner, R., Hong, F., Pellerin, M., Danas, K., 2018. Random distribution of polydisperse ellipsoidal inclusions and homogenization estimates for porous elastic materials. Comput. Struct. 210, 87–101. http://dx.doi.org/10.1016/j.compstruc.2018.08.006.

Avellaneda, M., 1987. Iterated homogenization, differential effective medium theory and applications. Comm. Pure Appl. Math. 40 (5), 527–554. http://dx.doi.org/10.1002/cpa.3160400502.

Barsoum, I., Faleskog, J., 2007. Rupture mechanisms in combined tension and shear—Micromechanics. Int. J. Solids Struct. 44 (17), 5481–5498. http://dx.doi.org/10.1016/j.ijsolstr.2007.01.010.

Bele, E., Deshpande, V.S., 2015. The compressive response of idealized cermetlike materials. J. Appl. Mech. 82 (4), http://dx.doi.org/10.1115/1.4029782.

Bele, E., Goel, A., Pickering, E., Borstnar, G., Katsamenis, O., Pierron, F., Danas, K., Deshpande, V., 2017. Deformation mechanisms of idealised cermets under multiaxial loading. J. Mech. Phys. Solids 102, 80–100. http://dx.doi.org/10.1016/j.jmps.2017.01.002.

Bouchart, V., Brieu, M., Kondo, D., Abdelaziz, M.N., 2008. Implementation and numerical verification of a non-linear homogenization method applied to hyperelastic composites. Comput. Mater. Sci. 43 (4), 670–680. http://dx.doi.org/10.1016/j.commatsci.2008.01.033.

Brassart, L., Inglis, H., Delannay, L., Doghri, I., Geubelle, P., 2009. An extended Mori–Tanaka homogenization scheme for finite strain modeling of debonding in particle-reinforced elastomers. Comput. Mater. Sci. 45 (3), 611–616. http://dx.doi.org/10.1016/j.commatsci.2008.06.021.

Bruggeman, V.D., 1935. Berechnung verschiedener physikalischer Konstanten von heterogenen Substanzen. I. Dielektrizitätskonstanten und Leitfähigkeiten der Mischkörper aus isotropen Substanzen. Ann. Phys. 416 (7), 636–664. http://dx.doi.org/10.1002/andp.19354160705.

Budiansky, B., 1965. On the elastic moduli of some heterogeneous materials. J. Mech. Phys. Solids 13 (4), 223–227. http://dx.doi.org/10.1016/0022-5096(65)90011-6.

Chi, H., Talischi, C., Lopez-Pamies, O., H. Paulino, G., 2015. Polygonal finite elements for finite elasticity. Internat. J. Numer. Methods Engrg. 101 (4), 305–328. http://dx.doi.org/10.1002/nme.4802.

Christensen, R., Lo, K., 1979. Solutions for effective shear properties in three phase sphere and cylinder models. J. Mech. Phys. Solids 27 (4), 315–330. http://dx.doi.org/10.1016/0022-5096(79)90032-2.

Danas, K., 2017. Effective response of classical, auxetic and chiral magnetoelastic materials by use of a new variational principle. J. Mech. Phys. Solids 105, 25–53. http://dx.doi.org/10.1016/j.jmps.2017.04.016.

DeBotton, G., Hariton, I., Socolsky, E., 2006. Neo-Hookean fiber-reinforced composites in finite elasticity. J. Mech. Phys. Solids 54 (3), 533–559. http://dx.doi.org/10.1016/j.jmps.2005.10.001.

Einstein, A., 1906. A new determination of molecular dimensions. Ann. Physics 19, 289–306. http://dx.doi.org/10.1002/andp.19063240204.

Eshelby, J.D., 1957. The determination of the elastic field of an ellipsoidal inclusion, and related problems. Proc. R. Soc. Lond. Ser. A Math. Phys. Sci. 241 (1226), 376–396. http://dx.doi.org/10.1098/rspa.1957.0133.

de Francqueville, F., Diani, J., Gilormini, P., Vandenbroucke, A., 2021. Use of micromechanical approach to understand the mechanical behavior of solid propellants. Mech. Mater. 153, 103656. http://dx.doi.org/10.1016/j.mechmat.2020.103656.

de Francqueville, F., Gilormini, P., Diani, J., 2019. Representative volume elements for the simulation of isotropic composites highly filled with monosized spheres. Int. J. Solids Struct. 158, 277–286. http://dx.doi.org/10.1016/j.ijsolstr.2018.09.013.

de Francqueville, F., Gilormini, P., Diani, J., Vandenbroucke, A., 2020. Relationship between local damage and macroscopic response of soft materials highly reinforced by monodispersed particles. Mech. Mater. 146, 103408. http://dx.doi.org/10.1016/j.mechmat.2020.103408.

Gangl, P., Sturm, K., Neunteufel, M., Schöberl, J., 2020. Fully and semi-automated shape differentiation in NGSolve. http://dx.doi.org/10.48550/ARXIV.2004.06783.

Geuzaine, C., Remacle, J.-F., 2009. Gmsh: A 3-D finite element mesh generator with built-in pre- and post-processing facilities. Internat. J. Numer. Methods Engrg. 79 (11), 1309–1331. http://dx.doi.org/10.1002/nme.2579.

Ghosh, K., Lefèvre, V., Lopez-Pamies, O., 2023. The effective shear modulus of a random isotropic suspension of monodisperse liquid n-spheres: from the dilute limit to the percolation threshold. Soft Matter 19 (2), 208–224. http://dx.doi.org/10.1039/d2sm01219g.

Goudarzi, T., Spring, D.W., Paulino, G.H., Lopez-Pamies, O., 2015. Filled elastomers: A theory of filler reinforcement based on hydrodynamic and interphasial effects. J. Mech. Phys. Solids 80, 37–67. http://dx.doi.org/10.1016/j.jmps.2015.04.012.

Guo, Z., Peng, X., Moran, B., 2007. Large deformation response of a hyperelastic fibre reinforced composite: Theoretical model and numerical validation. Composites A 38 (8), 1842–1851. http://dx.doi.org/10.1016/j.compositesa.2007.04.004.

Guo, Z., Shi, X., Chen, Y., Chen, H., Peng, X., Harrison, P., 2014. Mechanical modeling of incompressible particle-reinforced neo-Hookean composites based on numerical homogenization. Mech. Mater. 70, 1–17. http://dx.doi.org/10.1016/j.mechmat.2013.11.004.

Gusev, A.A., 2016. Controlled accuracy finite element estimates for the effective stiffness of composites with spherical inclusions. Int. J. Solids Struct. 80, 227–236. http://dx.doi.org/10.1016/j.ijsolstr.2015.11.006.

Hashin, Z., 1985. Large isotropic elastic deformation of composites and porous media. Int. J. Solids Struct. 21 (7), 711–720. http://dx.doi.org/10.1016/0020-7683(85)90074-5.

Hashin, Z., Shtrikman, S., 1961. Note on a variational approach to the theory of composite elastic materials. J. Franklin Inst. B 271 (4), 336–341. http://dx.doi.org/10.1016/0016-0032(61)90032-1.

Hashin, Z., Shtrikman, S., 1963. A variational approach to the theory of the elastic behaviour of multiphase materials. J. Mech. Phys. Solids 11 (2), 127–140. http://dx.doi.org/10.1016/0022-5096(63)90060-7.

Hooshmand-Ahoor, Z., Tarantino, M., Danas, K., 2022. Mechanically-grown morphogenesis of Voronoi-type materials: Computer design, 3D-printing and experiments. Mech. Mater. 173, 104432. http://dx.doi.org/10.1016/j.mechmat.2022.104432.

Jiménez, F.L., 2016. On the isotropy of randomly generated representative volume elements for fiber-reinforced elastomers. Composites B 87, 33–39. http://dx.doi.org/10.1016/j.compositesb.2015.10.014.

Jiménez, F.L., Pellegrino, S., 2012. Constitutive modeling of fiber composites with a soft hyperelastic matrix. Int. J. Solids Struct. 49 (3–4), 635–647. http://dx.doi.org/10.1016/j.ijsolstr.2011.11.006.

Kari, S., Berger, H., Rodriguez-Ramos, R., Gabbert, U., 2007. Computational evaluation of effective material properties of composites reinforced by randomly distributed spherical particles. Compos. Struct. 77 (2), 223–231. http://dx.doi.org/10.1016/j.compstruct.2005.07.003.

Khisaeva, Z., Ostoja-Starzewski, M., 2006. On the size of RVE in finite elasticity of random composites. J. Elasticity 85 (2), 153–173. http://dx.doi.org/10.1007/s10659-006-9076-y.

Kumar, S., Danas, K., Kochmann, D.M., 2019. Enhanced local maximum-entropy approximation for stable meshfree simulations. Comput. Methods Appl. Mech. Engrg. 344, 858–886. http://dx.doi.org/10.1016/j.cma.2018.10.030.

Lefèvre, V., Francfort, G.A., Lopez-Pamies, O., 2022. The curious case of 2D isotropic incompressible Neo-Hookean composites. J. Elasticity 151 (1), 177–186. http://dx.doi.org/10.1007/s10659-022-09907-2.

Lefèvre, V., Lopez-Pamies, O., 2014. The overall elastic dielectric properties of a suspension of spherical particles in rubber: An exact explicit solution in the small-deformation limit. J. Appl. Phys. 116 (13), 134106. http://dx.doi.org/10.1063/1.4897199.

Lefèvre, V., Lopez-Pamies, O., 2015. The overall elastic dielectric properties of fiber-strengthened/weakened elastomers. J. Appl. Mech. 82 (11), http://dx.doi.org/10.1115/1.4031187.

Lefèvre, V., Lopez-Pamies, O., 2022. The effective shear modulus of a random isotropic suspension of monodisperse rigid n-spheres: From the dilute limit to the percolation threshold. Extreme Mech. Lett. 55, 101818. http://dx.doi.org/10.1016/j.eml.2022.101818.

Leger, S., Fortin, A., Tibirna, C., Fortin, M., 2014. An updated Lagrangian method with error estimation and adaptive remeshing for very large deformation elasticity problems. Internat. J. Numer. Methods Engrg. 100, 1006–1030. http://dx.doi.org/10.1002/nme.4786.

Leonard, M., Wang, N., Lopez-Pamies, O., Nakamura, T., 2020. The nonlinear elastic response of filled elastomers: Experiments vs. theory for the basic case of particulate fillers of micrometer size. J. Mech. Phys. Solids 135, 103781. http://dx.doi.org/10.1016/j.jmps.2019.103781.

Lopez-Pamies, O., Goudarzi, T., Danas, K., 2013. The nonlinear elastic response of suspensions of rigid inclusions in rubber: II—A simple explicit approximation for finite-concentration suspensions. J. Mech. Phys. Solids 61 (1), 19–37. http://dx.doi.org/10.1016/j.jmps.2012.08.013.

Lopez-Pamies, O., Ponte Castañeda, P., 2006. On the overall behavior, microstructure evolution, and macroscopic stability in reinforced rubbers at large deformations: I—Theory. J. Mech. Phys. Solids 54 (4), 807–830. http://dx.doi.org/10.1016/j.jmps.2005.10.006.

Lopez-Pamies, O., Ponte Castañeda, P., 2007. Homogenization-based constitutive models for porous elastomers and implications for macroscopic instabilities: I—Analysis. J. Mech. Phys. Solids 55 (8), 1677–1701. http://dx.doi.org/10.1016/j.jmps.2007.01.007.

Lubachevsky, B.D., Stillinger, F.H., 1990. Geometric properties of random disk packings. J. Stat. Phys. 60 (5–6), 561–583. http://dx.doi.org/10.1007/bf01025983.

Matsuda, A., Watanabe, O., de Borst, R., 2004. The stress-rate of hyperelasticity based on the updated Lagrangian formulation. JSME Int. J. A47, 164–172. http://dx.doi.org/10.1299/jsmea.47.164.

Mbiakop, A., Constantinescu, A., Danas, K., 2015. An analytical model for porous single crystals with ellipsoidal voids. J. Mech. Phys. Solids 84, 436–467. http://dx.doi.org/10.1016/j.jmps.2015.07.011.

Meng, Q., Wang, Z., 2015. Prediction of interfacial strength and failure mechanisms in particle-reinforced metal-matrix composites based on a micromechanical model. Eng. Fract. Mech. 142, 170–183. http://dx.doi.org/10.1016/j.engfracmech.2015.06.001.

Michel, J., Lopez-Pamies, O., Ponte Castañeda, P., Triantafyllidis, N., 2007. Microscopic and macroscopic instabilities in finitely strained porous elastomers. J. Mech. Phys. Solids 55 (5), 900–938. http://dx.doi.org/10.1016/j.jmps.2006.11.006.

Michel, J., Moulinec, H., Suquet, P., 1999. Effective properties of composite materials with periodic microstructure: a computational approach. Comput. Methods Appl. Mech. Engrg. 172 (1–4), 109–143. http://dx.doi.org/10.1016/s0045-7825(98)00227-8.

Moraleda, J., Segurado, J., LLorca, J., 2009. Finite deformation of incompressible fiber-reinforced elastomers: A computational micromechanics approach. J. Mech. Phys. Solids 57 (9), 1596–1613. http://dx.doi.org/10.1016/j.jmps.2009.05.007.

Mukherjee, D., Bodelot, L., Danas, K., 2020. Microstructurally-guided explicit continuum models for isotropic magnetorheological elastomers with iron particles. Int. J. Non-Linear Mech. 120, 103380. http://dx.doi.org/10.1016/j.ijnonlinmec.2019.103380.

Mukherjee, D., Rambausek, M., Danas, K., 2021. An explicit dissipative model for isotropic hard magnetorheological elastomers. J. Mech. Phys. Solids 151, 104361. http://dx.doi.org/10.1016/j.jmps.2021.104361.

Neumann, M., Stenzel, O., Willot, F., Holzer, L., Schmidt, V., 2020. Quantifying the influence of microstructure on effective conductivity and permeability: Virtual materials testing. Int. J. Solids Struct. 184, 211–220. http://dx.doi.org/10.1016/j.ijsolstr.2019.03.028.

Norris, A., 1985. A differential scheme for the effective moduli of composites. Mech. Mater. 4 (1), 1–16. http://dx.doi.org/10.1016/0167-6636(85)90002-x.

Pickering, E., Bele, E., Deshpande, V., 2016. Multi-axial response of idealized cermets. Acta Mater. 116, 281–289. http://dx.doi.org/10.1016/j.actamat.2016.06.051.

Rudland, D., Wilkowski, G., Wang, Y.-Y., Norris, W., 2004. Development of circumferential through-wall crack K-solutions for control rod drive mechanism nozzles. Int. J. Press. Vessels Pip. 81 (12), 961–971. http://dx.doi.org/10.1016/j.ijpvp.2004.04.003.

Schöberl, J., 1997. NETGEN An advancing front 2D/3D-mesh generator based on abstract rules. Comput. Vis. Sci. 1 (1), 41–52. http://dx.doi.org/10.1007/s007910050004.

Scott, G.D., 1960. Packing of spheres: Packing of equal spheres. Nature 188 (4754), 908–909. http://dx.doi.org/10.1038/188908a0.

Segurado, J., Llorca, J., 2002. A numerical approximation to the elastic properties of sphere-reinforced composites. J. Mech. Phys. Solids 50 (10), 2107–2121. http://dx.doi.org/10.1016/s0022-5096(02)00021-2.

Shrimali, B., Lefèvre, V., Lopez-Pamies, O., 2019. A simple explicit homogenization solution for the macroscopic elastic response of isotropic porous elastomers. J. Mech. Phys. Solids 122, 364–380. http://dx.doi.org/10.1016/j.jmps.2018.09.026.

Shrimali, B., Parnell, W.J., Lopez-Pamies, O., 2020. A simple explicit model constructed from a homogenization solution for the large-strain mechanical response of elastomeric syntactic foams. Int. J. Non-Linear Mech. 126, 103548. http://dx.doi.org/10.1016/j.ijnonlinmec.2020.103548.

Spring, D.W., Paulino, G.H., 2014. A growing library of three-dimensional cohesive elements for use in ABAQUS. Eng. Fract. Mech. 126, 190–216. http://dx.doi.org/10.1016/j.engfracmech.2014.04.004.

Spyrou, L., Agoras, M., Danas, K., 2017. A homogenization model of the Voigt type for skeletal muscle. J. Theoret. Biol. 414, 50–61. http://dx.doi.org/10.1016/j.jtbi.2016.11.018.

Spyrou, L., Brisard, S., Danas, K., 2019. Multiscale modeling of skeletal muscle tissues based on analytical and numerical homogenization. J. Mech. Behav. Biomed. Mater. 92, 97–117. http://dx.doi.org/10.1016/j.jmbbm.2018.12.030.

Tarantino, M., Mortensen, A., 2022. On the bulk compressibility of close-packed particles and their composites. Composites A 161, 107106. http://dx.doi.org/10.1016/j.compositesa.2022.107106.

Tarantino, M., Weber, L., Mortensen, A., 2016. Effect of hydrostatic pressure on flow and deformation in highly reinforced particulate composites. Acta Mater. 117, 345–355. http://dx.doi.org/10.1016/j.actamat.2016.06.052.

Tarantino, M., Zerhouni, O., Danas, K., 2019. Random 3D-printed isotropic composites with high volume fraction of pore-like polydisperse inclusions and near-optimal elastic stiffness. Acta Mater. 175, 331–340. http://dx.doi.org/10.1016/j.actamat.2019.06.020.

Torquato, S., Stillinger, F.H., 2010. Jammed hard-particle packings: From Kepler to Bernal and beyond. Rev. Modern Phys. 82 (3), 2633–2672. http://dx.doi.org/10.1103/revmodphys.82.2633.

Travers, T., Ammi, M., Bideau, D., Gervois, A., Messager, J.C., Troadec, J.P., 1987. Uniaxial compression of 2d packings of cylinders. Effects of weak disorder. Europhys. Lett. 4 (3), 329. http://dx.doi.org/10.1209/0295-5075/4/3/012.

Wang, C.G., Chen, C., Wang, W., Shi, H.B., Liu, H.C., 2011. Remeshing technique for three dimensional finite element in ABAQUS. Appl. Mech. Mater. 71–78, 4147–4150. http://dx.doi.org/10.4028/www.scientific.net/amm.71-78.4147.

Willot, F., Jeulin, D., 2009. Elastic behavior of composites containing Boolean random sets of inhomogeneities. Internat. J. Engrg. Sci. 47 (2), 313–324. http://dx.doi.org/10.1016/j.ijengsci.2008.09.016.

Yang, P., Guo, Z., Hu, N., Sun, W., Chen, Y., 2022. Hyperelastic behaviors of closed-cell porous materials at a wide porosity range. Compos. Struct. 294, 115792. http://dx.doi.org/10.1016/j.compstruct.2022.115792.

Yang, Q., Xu, F., 2009. Numerical modeling of nonlinear deformation of polymer composites based on hyperelastic constitutive law. Front. Mech. Eng. China 4 (3), 284–288. http://dx.doi.org/10.1007/s11465-009-0067-0.

Yuan, W.-H., Wang, H.-C., Zhang, W., Dai, B.-B., Liu, K., Wang, Y., 2021. Particle finite element method implementation for large deformation analysis using Abaqus. Acta Geotech. 16 (8), 2449–2462. http://dx.doi.org/10.1007/s11440-020-01124-2.

Zerhouni, O., Brisard, S., Danas, K., 2021. Quantifying the effect of two-point correlations on the effective elasticity of specific classes of random porous materials with and without connectivity. Internat. J. Engrg. Sci. 166, 103520. http://dx.doi.org/10.1016/j.ijengsci.2021.103520.

Zerhouni, O., Tarantino, M., Danas, K., 2019. Numerically-aided 3D printed random isotropic porous materials approaching the Hashin-Shtrikman bounds. Composites B 156, 344–354. http://dx.doi.org/10.1016/j.compositesb.2018.08.032.